Hybridization of FDTD and Device Behavioral-Modeling Techniques

Hybridization of FDTD and Device Behavioral-Modeling Techniques

Stefano Grivet-Talocia, Igor S. Stievano, and Flavio G. Canavero, *Senior Member, IEEE*

***Abstract*—We present a systematic methodology for the electromagnetic modeling of interconnected digital I/O ports. Digital drivers and receivers are represented through behavioral models based on radial basis functions expansions. Such a technique allows a very accurate representation of nonlinear/dynamic effects as well as switching behavior of real-world components by means of carefully identified discrete-time models. The inclusion of these models into a finite-difference time-domain solver for full-wave analysis of interconnected systems is presented. A rigorous stability analysis shows that use of nonlinear/dynamic discrete-time models can be easily integrated with standard full-wave solvers, even in the case of unmatched sampling time. A set of numerical examples illustrates the feasibility of this method.**

***Index Terms*—Behavioral models, digital I/O ports, finite-difference time-domain (FDTD) methods, nonlinear circuits, radial basis functions, transient analysis.**

I. Introduction

THE high complexity of modern electronic systems requires careful modeling strategies at early stages of the design process. This is particularly important for the characterization of interconnected structures loaded by digital drivers and receivers. Indeed, it is well known that electromagnetic compatibility (EMC) and signal integrity (SI) are strongly affected by the geometry of the interconnects and by the possibly complex nonlinear/dynamic behavior of the electronic devices collocated at their terminations. An accurate solver must combine a rigorous full-wave scheme together with precise models of digital ports. The strong nonlinearities and the dynamic behavior are correctly represented by a detailed transistor-level circuit, which is, however, too heavy to be considered for direct inclusion within a full-wave modeling tool.

Two main approaches for the simulation of a loaded interconnected structure can be devised. One possibility is to retain the full complexity of the components using their transistor-level model, attempting the derivation of simple macromodels for the description of the signal propagation paths. This approach is particularly suited when the signals propagate along transmission lines with controlled geometry [e.g., parallel lands on printed circuit boards (PCBs)] or multichip modules (MCMs), since transmission-line models can be easily included within a SPICE-like circuit simulation environment. Accuracy breakdown occurs in the presence of discontinuities and complex geometries like vias, bends, cut power/ground planes, etc. [16]. In these cases, the quasi-TEM mode no longer represents the electromagnetic fields and full-wave modeling is required. It should be noted that also in this situation (reduced-order) macromodeling techniques based on equivalent multiport extraction from some three-dimensional (3-D) field discretization can be devised. The result is a global circuit description of components and propagation paths. This is a very active research area, as demonstrated by the large number of recent papers on the subject (see, e.g., [2], [3], [10] and references therein). We remark that this modeling strategy is best suited for pure SI analysis since only the port behavior of the structure at few selected locations is modeled.

This paper concentrates on a second complementary modeling strategy, which is better suited for EMC analysis including radiation and susceptibility from incident fields. A conventional field solver is used to discretize the electromagnetic fields within the computational domain. We concentrate herewith on the well-known finite-difference time-domain (FDTD) scheme [8], [22], [27] since it has become a standard in EMC modeling due to its simplicity and accuracy. Suitable models for the nonlinear/dynamic components loading the interconnects are inserted as lumped elements within the computational mesh. This procedure has been developed by several researchers during the past ten years. Application examples include single passive linear components (resistors, capacitors, inductors), voltage sources, simple nonlinear components (see, e.g., [9], [13], [21], [24]). More recently, this procedure has been extended to include linear multiports characterized by rational transfer functions [12], [26], lumped ferrites [6], and many other types of lumped components. For a review see [23] and references therein.

In this paper, we propose a systematic procedure for the behavioral description of nonlinear/dynamic effects of real-world digital I/O ports based on radial basis functions (RBF) expansions [18]–[20]. The device is modeled through a discrete-time nonlinear dynamic parametric macromodel leading to a virtually undistinguishable response under very different loading conditions with respect to the transistor-level model. The parameters are computed only once through a rigorous identification procedure and are used for all subsequent simulations.

There are several advantages beyond accuracy in this approach. The computational complexity required for the transient simulation of such a macromodel is much less than for the transistor level circuit. In addition, due to the intrinsic nature of the model representation, each device is represented by its own set of parameters. This allows the macromodel implementation

Manuscript received May 9, 2002; revised September 24, 2002.

The authors are with the Dipartimento di Elettronica, Politecnico di Torino, 10129, Turin, Italy (e-mail: grivet@polito.it).

Digital Object Identifier 10.1109/TEMC.2002.808035

to be quite general, since the same computational code can be used for very different devices simply feeding it with the proper model parameters. It is also conceivable to setup libraries of components that can be arbitrarily selected and included by the user.

The RBF macromodels used in this paper are discrete-time nonlinear models, consisting of a set of difference equations relating present and past samples of port voltage and current with fixed sampling time. The latter is usually defined in the model identification stage and is one of the key parameters that characterize the device. On the other hand, transient field solvers like FDTD often require a proper time step determined by the spatial mesh size through the Courant condition. Therefore, discrete-time macromodels can in principle be included within a FDTD mesh only if the model sampling time and the transient time step are matched. For this reason, we present in this paper a rigorous analysis of the resampling problem together with a stability analysis. This analysis allows us to conclude that the class of presented RBF models preserve stability also after resampling, and can therefore be used without additional constraints for full-wave simulations.

The outline of this paper is as follows. Section II discusses the inclusion of lumped device models within a 3-D FDTD mesh. Also, an incident/scattered field formulation is presented, allowing for electromagnetic susceptibility analysis of interconnected digital ports. Section III introduces discrete-time RBF models of digital I/O ports, while Section IV details the resampling strategy for time step matching between RBF models and FDTD. Section V details the FDTD implementation of the proposed RBF macromodels. Section VI presents validations and numerical results. The detailed theoretical analysis proving the stability of the overall modeling strategy is postponed to Appendix A and B in order to smooth the flow of presentation.

II. Full-Wave FDTD and Lumped Elements

This section recalls the main steps required by the inclusion of a lumped element within the FDTD computational domain. We remark that this is a standard procedure, therefore we only give an outline in order to set the notations that will be necessary throughout the paper. The reader is referred to the vast literature on the subject for further details.

We consider a locally uniform medium in the vicinity of the lumped element, with permettivity ε, permeability μ, and conductivity σ. The entire computational domain is discretized with a FDTD mesh size Δx, Δy, Δz along the three Cartesian coordinates. Without loss of generality we consider the situation illustrated in Fig. 1, with the lumped element collocated in the $\{i,j,k\}$ cell along the $\hat{z}$ coordinate. It is well known that the Maxwell-Ampere curl equation can be modified as

$$\nabla \times \mathbf{H} = \varepsilon \frac{\partial \mathbf{E}}{\partial t} + \sigma \mathbf{E} + \mathbf{J} \tag{1}$$

where $\mathbf{J}$ is the current density associated with the lumped element, which in turn can be expressed in terms of the current I_L as

$$\mathbf{J} = \frac{I_L}{\Delta x \Delta y}\,\hat{z}. \tag{2}$$

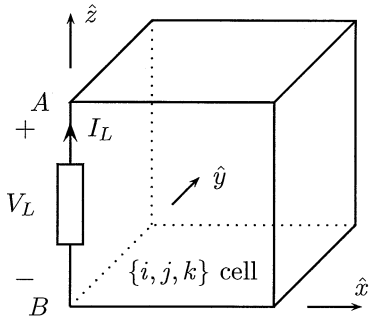

Fig. 1. Collocation of the lumped element in the FDTD mesh.

The lumped voltage V_L is expressed in terms of the electric field through

$$V_L = \int_A^B \mathbf{E} \cdot \hat{z}\, dz. \tag{3}$$

Taking the z-directed component from (1) and performing the standard FDTD discretization, we get after rearranging the various terms

$$\alpha_0 V_L^{n+1} - \alpha_1 V_L^n + \alpha_2 \left[\hat{z} \cdot \nabla \times \mathbf{H}\right]_{ijk}^{n+1/2} - \alpha_3 \left(I_L^{n+1} + I_L^n\right) = 0 \tag{4}$$

where superscript indicates the time iteration $t_n = n\Delta t$ and

$$\begin{aligned} \alpha_0 &= 1 + \frac{\sigma \Delta t}{2\varepsilon} \\ \alpha_1 &= 1 - \frac{\sigma \Delta t}{2\varepsilon} \\ \alpha_2 &= \frac{\Delta z \Delta t}{\varepsilon} \\ \alpha_3 &= \frac{\Delta z \Delta t}{2\varepsilon \Delta x \Delta y.} \end{aligned} \tag{5}$$

Note that a semi-implicit discretization of conduction current and lumped current density has been used in order to get an FDTD update equation that uses only the unknowns that are available on the space–time FDTD grid. Equation (4) must be coupled with the current-voltage characteristic of the lumped element in order to be solved for both V_L^{n+1} and I_L^{n+1}. All other quantities in (4) are known from previous iterations.

A. Incident Field Excitation

The update equation (4) can be easily modified to account for the contribution of an external field impinging on the structure. Several approaches can be adopted, the most convenient in present case being a scattered-field FDTD formulation [8]. Total fields are split in two separate contributions

$$\mathbf{E} = \mathbf{E}_i + \mathbf{E}_s \qquad \mathbf{H} = \mathbf{H}_i + \mathbf{H}_s. \tag{6}$$

The incident fields $\mathbf{E}_i, \mathbf{H}_i$ are distributed sources representing the fields that would be present in free space. These fields obey the free-space Maxwell equations, in particular

$$\nabla \times \mathbf{H}_i = \varepsilon_0 \frac{\partial \mathbf{E}_i}{\partial t} \tag{7}$$

and must be known *a priori*. The scattered fields $\mathbf{E}_s, \mathbf{H}_s$ are produced by the interaction of the incident fields with the con-

stitutive materials of the structure under investigation. Only the scattered fields are discretized in the FDTD mesh. The resulting form of Ampere–Maxwell curl equation may be obtained combining (7) with (1)

$$\nabla \times \mathbf{H}_s + \varepsilon_0 \frac{\partial \mathbf{E}_i}{\partial t} = \varepsilon \frac{\partial \mathbf{E}}{\partial t} + \sigma \mathbf{E} + \mathbf{J}\,. \tag{8}$$

Note that we have preserved the total electric field in order to define properly the port voltage V_L through (3). Equation (8) is identical to (1) except for the presence of the distributed source term related to the incident field. Therefore, following the same discretization procedure used in the case of no incident field, we get

$$\alpha_0 V_L^{n+1} - \alpha_1 V_L^n + \alpha_2 \left[\hat{z} \cdot \nabla \times \mathbf{H}_s\right]_{ijk}^{n+1/2} + \alpha_2 \varepsilon_0 \left.\frac{\partial E_{i,z}}{\partial t}\right|_{ijk}^{n+1/2} - \alpha_3 \left(I_L^{n+1} + I_L^n\right) = 0\,. \tag{9}$$

Once this expression is coupled to the lumped element current-voltage characteristic and solved, the scattered electric field can be computed as

$$\mathbf{E}_s^{n+1} = -\mathbf{E}_i^{n+1} - \frac{V_L^{n+1}}{\Delta z}\,. \tag{10}$$

The above is needed for the subsequent evaluation of the scattered fields in the adjacent cells.

III. Macromodels of Digital I/O Ports

A. Parametric Macromodeling

This section gives a short description of the parametric macromodels developed for digital I/O ports that will be adopted in the forthcoming sections. A more complete presentation can be found in [18], so we will outline only the main concepts that are strictly necessary for readability.

Digital I/O ports provide an interface between the internal structure of integrated circuits (IC) and the external interconnects carrying signals. The proposed macromodeling approach neglects the internal activity of the IC core, regarded as a black-box, and concentrates only on the electrical characteristics of the ports loading the interconnects. These can be identified by output ports of drivers and input ports of receivers and act as possibly complex nonlinear/dynamic time-varying terminations for the interconnects. In the typical case of a digital driver, this modeling strategy is justified since the internal IC logic activity forces different bit patterns at the output port. Such patterns can be assumed as known *a priori*. Conversely, once the bit pattern is fixed, the (analog) port voltage and current transient waveforms are mostly an intrinsic feature of the output stage of the driver. Only the latter needs careful modeling and will be investigated in the following. The same considerations apply for input ports of digital receivers.

The common way to build macromodels for digital I/O ports is via the definition of simplified equivalent circuits. Such equivalents allow physical insight and facilitate the implementation of the models. An important example of the equivalent circuit approach is provided by the widely adopted input–output buffer information specification (IBIS) [4], that has given rise to a large set of dedicated libraries for the electronic design automation tools. However, such an approach has also some inherent limitations. Mainly, the effects taken into account must be decided a priori by choosing a specific topology for the equivalent circuits.

The alternative approach we propose amounts to looking for parametric macromodels suitable for the description of the external port behavior of the device under modeling. The device is represented by a mathematical model relating samples of port voltage and current. The specific form of the model equations is chosen with the aid of the well established theory of system identification [7] and is detailed below. The model parameters are computed with a standard procedure by fitting the predicted macromodel response to some reference response obtained by driving the port with suitable stimuli. The parametric approach has interesting advantages, that makes it a useful complement to the more traditional equivalent circuit approach. It automatically takes into account any physical effects significantly influencing voltages and currents of the I/O ports, yielding models that perform at a very good accuracy level with relatively high efficiency. In addition, the accuracy of the models turns out to be weakly sensitive to the driven load. Finally, if needed, the parametric approach allows the creation of behavioral models from actually measured input-output transient waveforms [20].

B. RBF Macromodels

Let us consider the voltage and current waveforms $v(t)$ and $i(t)$ of some digital I/O port under test. All the macromodels considered in this paper are discrete-time models, therefore, we sample the time axis with given sampling time T_s. This sampling time must be carefully determined on the basis of the dynamic features of the device. In particular, T_s is not related to the FDTD sampling time Δt, which is constrained by the adopted spatial discretization. In order to avoid confusion, we will use a different time index m for quantities that are sampled at T_s rate. All issues related to discrete-time resampling for time step matching between RBF model and FDTD will be addressed in Section IV.

Under the above assumptions, we will indicate the voltage and current samples as

$$v^m = v(mT_s) \quad i^m = i(mT_s)\,. \tag{11}$$

A general form of parametric macromodel for the device can be expressed as [7]

$$i^m = F(\boldsymbol{\Theta}; \mathbf{x}_i^{m-1}, v^m, \mathbf{x}_v^{m-1}; m) \tag{12}$$

where $\mathbf{x}_v^{m-1}$ and $\mathbf{x}_i^{m-1}$ are regressor vectors collecting the past r voltage and current samples

$$\begin{aligned} \mathbf{x}_v^{m-1} &= \left[v^{m-1}, v^{m-2}, \ldots, v^{m-r}\right]^T \\ \mathbf{x}_i^{m-1} &= \left[i^{m-1}, i^{m-2}, \ldots, i^{m-r}\right]^T\,. \end{aligned} \tag{13}$$

These vectors act as discrete-time internal states of the model, with r indicating its dynamic order. The function F is a nonlinear mapping from $\Re^{2r+1}$ to $\Re$ defining the *model represen-*

tation and $\boldsymbol{\Theta}$ is the vector of model parameters, defining the *model structure*. Note that F depends also on time m, since digital drivers must be modeled as time-varying components in order to capture switching behavior.

In this paper, we mainly concentrate on model representations F defined by Gaussian RBF expansions [1], [5], [17]. Such representations provide approximations of the mapping F through expansion into L multivariate Gaussian functions of suitable width β centered at appropriate points $\mathbf{c}$ in the regressor space of dimension $2r+1$. A general form of such representation can be expressed by

$$F(\boldsymbol{\Theta}, \mathbf{x}_i^{m-1}, v^m, \mathbf{x}_v^{m-1}) = \sum_{l=1}^{L} \theta_l \, \Psi_l(m-1) \, \exp\left\{-\frac{(v^m - c_l^0)^2}{2\beta^2}\right\} \quad (14)$$

where the term $\Psi_l(m-1)$ collects all contributions due to past voltage and current samples

$$\Psi_l(m-1) = \exp\left\{-\frac{\|\mathbf{x}_i^{m-1} - \mathbf{c}_l^i\|^2 + \|\mathbf{x}_v^{m-1} - \mathbf{c}_l^v\|^2}{2\beta^2}\right\} \quad (15)$$

and $\|\cdot\|$ denotes the Euclidean norm. The model parameters are

$$\boldsymbol{\Theta} = \left[\theta_1, \ldots, \theta_L; \mathbf{c}_1^{iT}, c_1^0, \mathbf{c}_1^{vT}, \ldots, \mathbf{c}_L^{iT}, c_L^0, \mathbf{c}_L^{vT}; \beta\right]^T . \quad (16)$$

The RBF representations can be applied to a wide range of modeling problems, as they lead to general results on the existence on nonlinear parametric models [14], [15]. They are numerically efficient (the evaluation of an expansion term requires the evaluation of norms in the multidimensional regressor space plus scalar functions) and the estimation of their parameters is easier than for other representations [1], [5]. Besides, the Gaussian RBF have local support. This feature further simplifies the parameter estimation and leads to asymptotically vanishing models. From a practical point of view, Gaussian RBF representations are well suited for digital I/O ports, as they can produce a model meeting the accuracy and efficiency specification of real simulation problems, at a low modeling cost. The following two sections particularize the general form of RBF model to digital output ports (drivers) and input ports (receivers). A specific example of RBF macromodeling applied to a real device is reported in Section VI.A for illustration purposes.

C. Drivers

One of the main difficulties in macromodeling output ports of drivers arises from the time-varying nature of the devices due to switching. Our proposed strategy amounts to using two separate Gaussian RBF submodels accounting for both static and dynamic effects of the port behavior at a fixed logic state, henceforth labeled i_u^m for the HIGH and i_d^m for the LOW state. These two submodels are time invariant. A piecewise-linear combination through time-varying weight functions $w_{u,d}^m$ provides a model for the evolution of the port logic state, acting as a switch between submodels $i_{u,d}^m$. The general RBF representation (14) is then specialized as

$$\begin{cases} i^m = & w_u^m i_u^m + w_d^m i_d^m \\ i_u^m = & \sum_{l=1}^{L_u} \theta_{ul} \, \Psi_{ul}(m-1) \, \exp\left\{-\frac{(v^m - c_{ul}^0)^2}{2\beta_u^2}\right\} \\ i_d^m = & \sum_{l=1}^{L_d} \theta_{dl} \, \Psi_{dl}(m-1) \, \exp\left\{-\frac{(v^m - c_{dl}^0)^2}{2\beta_d^2}\right\}. \end{cases} \quad (17)$$

A more detailed discussion on the systematic derivation of model (17) together with guidelines for the estimation of its parameters can be found in [18].

D. Receivers

Macromodeling of receivers input ports follows a similar approach to that used for drivers. However, receivers are not time-varying components, therefore simpler models can be devised. The proposed structure for a receiver model is

$$i^m = i_{\text{lin}}^m + i_{\text{nl},u}^m + i_{\text{nl},d}^m \quad (18)$$

where i_{lin}^m is a linear parametric submodel accounting for the mainly linear behavior of the port for voltage values within the range of the power supply voltage, while $i_{\text{nl},u}^m$ and $i_{\text{nl},d}^m$ are Gaussian RBF submodels taking into account both the nonlinear static and dynamic effects of the up and the down protection circuits, respectively. Since receiver macromodels are somewhat simpler than driver models, we will focus our attention on the latter in the forthcoming sections.

IV. Resampling

In Section III, we presented the general form of a discrete-time parametric model [see (12)] that can be applied for an effective behavioral description of fast digital drivers and receivers. One of the key parameters of such model is the sampling time T_s used in the identification stage. The model dynamic equations strongly depend on this sampling time, since the internal states $\{\mathbf{x}_v, \mathbf{x}_i\}$ collect past samples of voltages and currents delayed by multiples of T_s. The numerical simulation of the model equations appears then to be constrained to use this sampling time. However, if this model is to be combined with an FDTD code as a lumped element, some problems might occur due to the Courant condition, which limits the time step Δt to a maximum value depending on the spatial dimensions of the FDTD cells. This section is devoted to a detailed analysis of the resampling procedure to be applied to the parameteric model (12) in order to match its sampling time to the one determined by the FDTD mesh. We present herewith the proposed resampling procedure, postponing the stability analysis to Appendix B.

Resampling can be viewed as a two-step process. First, the discrete-time model is converted into a continuous-time model. Then, a suitable time discretization scheme is applied to get a resampled model. Conversion of (12) to continuous time requires the derivation of a system of state equations with appropriate dynamic order. Since r past samples of both voltage and current are involved in the discrete-time equations [see (13)], we will use a global dynamic order $2r$ also for the continuous-time

model. The continuous state variables $\{\mathbf{y}_v, \mathbf{y}_i\}$ will be delayed voltages and currents, defined componentwise as

$$y_{v,p}(t) = v(t-pT_s) \quad y_{i,p}(t) = i(t-pT_s), \qquad p = 1, \ldots, r\,. \tag{19}$$

Note that the following equivalences between continuous-time and discrete-time states hold:

$$\mathbf{y}_v(mT_s) = \mathbf{x}_v^{m-1} \quad \mathbf{y}_i(mT_s) = \mathbf{x}_i^{m-1}. \tag{20}$$

Subtracting now $i^{m-1} = i([m-1]T_s) = x_{i,1}^{m-1}$ from (12) and dividing by T_s we get

$$\frac{i^m - i^{m-1}}{T_s} = \frac{1}{T_s}\left\{F(\boldsymbol{\Theta}; \mathbf{x}_i^{m-1}, v^m, \mathbf{x}_v^{m-1}; m) - x_{i,1}^{m-1}\right\}. \tag{21}$$

The left-hand side is easily identified with a first-order forward approximation of the time derivative of the port current at time $(m-1)T_s$, i.e., of the first continuous state variable $y_{i,1}$. Replacing this finite-difference approximation with the time derivative and passing to continuous time $t \leftrightarrow mT_s$ we get the first continuous-state equation

$$\frac{d}{dt}y_{i,1}(t) = \frac{1}{T_s}\left\{F(\boldsymbol{\Theta}; \mathbf{y}_i(t), v(y), \mathbf{y}_v(t); t) - y_{i,1}(t)\right\}. \tag{22}$$

The leading error term in this approximation is $O(T_s^2)$. The same procedure can be applied to the other state variables. For instance, we get for the second current state

$$\frac{d}{dt}y_{i,2}(t) = \frac{1}{T_s}\left(y_{i,1}(t) - y_{i,2}(t)\right) \tag{23}$$

and similarly for all the other current and voltage states. After a straightforward algebraic manipulation we get the final continuous-time model

$$\begin{cases} \frac{d}{dt}\mathbf{y}_i(t) &= \frac{1}{T_s}\,\mathbf{A}_r\,\mathbf{y}_i(t) + \frac{1}{T_s}\,\mathbf{e}_r\,F(\boldsymbol{\Theta}; \mathbf{y}_i(t), v(t), \mathbf{y}_v(t); t) \\ \frac{d}{dt}\mathbf{y}_v(t) &= \frac{1}{T_s}\,\mathbf{A}_r\,\mathbf{y}_v(t) + \frac{1}{T_s}\,\mathbf{e}_r\,v(t) \\ i(t) &= F(\boldsymbol{\Theta}; \mathbf{y}_i(t), v(t), \mathbf{y}_v(t); t) \end{cases} \tag{24}$$

where $\mathbf{A}_r$ is the $r \times r$ matrix

$$\mathbf{A}_r = \begin{bmatrix} -1 & 0 & \ldots & 0 \\ 1 & -1 & \ldots & 0 \\ \vdots & \ddots & \ddots & \vdots \\ 0 & \ldots & 1 & -1 \end{bmatrix} \tag{25}$$

and $\mathbf{e}_r = (1, 0, \ldots, 0)^T$. The first two rows represent the actual state equations with dynamic order $2r$, and the third row represents the output equation relating the port current to the port voltage and the internal states.

The continuous-time system can be easily synthesized into a SPICE equivalent circuit for automatic analysis under given loading conditions. Details of such implementation can be found in [18]. During a transient simulation SPICE will perform a time-domain discretization, using a high-order method with variable time step. It is then expected that a SPICE simulation will give results very close to the true solution of the continuous-time model. The numerical results of [18] illustrate that this solution is indeed almost undistinguishable from the response of the transistor-level circuit describing the original device. This means that the combination of RBF model identification and discrete-to-continuous time conversion constitute a very stable and accurate algorithm.

We proceed now to the discretization of system (24) by using the new (FDTD-related) sampling time Δt. Henceforth, we will indicate with

$$\tau = \frac{\Delta t}{T_s} \tag{26}$$

the resampling factor. Consistently with the first-order approximation that led to the construction of the continuous-time system from the original discrete-time model, we approximate the time derivative with a first-order forward finite difference

$$\left.\frac{d}{dt}f(t)\right|_{t=n\Delta t} \simeq \frac{f([n+1]\Delta t) - f(n\Delta t)}{\Delta t}\,. \tag{27}$$

Note that we are using a different index n for the resampled time axis. The resulting resampled model reads

$$\begin{cases} \mathbf{x}_i^{n+1} &= [\mathbf{I}_r + \tau\mathbf{A}_r]\,\mathbf{x}_i^n + \tau\,\mathbf{e}_r\,F(\boldsymbol{\Theta}; \mathbf{x}_i^n, v^n, \mathbf{x}_v^n; n) \\ \mathbf{x}_v^{n+1} &= [\mathbf{I}_r + \tau\mathbf{A}_r]\,\mathbf{x}_v^n + \tau\,\mathbf{e}_r\,v^n \\ i^n &= F(\boldsymbol{\Theta}; \mathbf{x}_i^n, v^n, \mathbf{x}_v^n; n) \end{cases} \tag{28}$$

where $\mathbf{I}_r$ is the $r \times r$ identity matrix. Note that, due to the employed forward difference approximation of the time derivative, the resampled state equations (first two rows of (28)) are explicit, while the nonlinear output equation (third row) is implicit. We will see in the Appendix that this feature allows us to preserve stability in the various time conversion steps. Also, note that the resampled system is identical to the original discrete system (12) when $\Delta t = T_s$, i.e., $\tau = 1$. In such case the state equations reduce to simple forward shifts in time by a T_s step.

V. FDTD Implementation of Lumped RBF Macromodels

This section combines the FDTD formulation with lumped elements detailed in Section II with the resampled RBF models discussed in Section IV. The result will be the complete FDTD implementation of RBF macromodels for digital I/O ports. Without loss of generality, we will focus our attention on the RBF driver model discussed in Section III-C, and we will detail the important issues related to the inclusion in the FDTD grid. A similar procedure can be used for the simpler case of an RBF receiver model.

We begin noting that two different sets of update equations are needed. One set is related to the update of the discrete-time states hidden in the device macromodel. This set of equations is readily obtained by particularizing the first two rows of (28) to the driver case, i.e., using two different dynamic RBF submodels for the two logic states of the device. The resulting update equations remain fully explicit in their unknowns and are consequently straightforward to implement. The second set of update equations is obtained by merging (4) with the resampled discrete-time driver characteristic. The latter is readily obtained by considering the nonlinear output equation [(the third row of (28)] and particularizing it to the driver case. The resulting nonlinear system reads as shown in (29) at the bottom

of the page which can be stated formally as $\mathbf{F}(\xi^{n+1}) = 0$, where the unknowns have been collected in the array $\xi^{n+1} = [V_L^{n+1}, I_u^{n+1}, I_d^{n+1}]^T$.

System (29) can be solved iteratively using, e.g., the Newton–Raphson method [25]

$$\xi_{p+1}^{n+1} = \xi_p^{n+1} - \left[\mathbf{M}_p^{n+1}\right]^{-1} \mathbf{F}(\xi_p^{n+1}) \tag{30}$$

where p indicates the iteration count and $\mathbf{M}$ is the Jacobian matrix of $\mathbf{F}$. Iterations are stopped when some accuracy threshold is reached. The initial guess ξ_0^{n+1} for starting the iterations can be conveniently taken as the solution ξ^n at previous time step, since it is expected that the time step Δt is small enough for producing a smooth solution. A convenient feature of this method is that the Jacobian matrix and its inverse can be computed analytically using the RBF model expression. Specifically

$$\left[\mathbf{M}_r^{n+1}\right]^{-1} = \frac{1}{\left|\mathbf{M}_r^{n+1}\right|} \times \begin{bmatrix} 1 & \alpha_3 w_u^{n+1} & \alpha_3 w_d^{n+1} \\ -Q_{u,r}^{n+1} & \alpha_0 + \alpha_3 w_d^{n+1} Q_{d,r}^{n+1} & -\alpha_3 w_d^{n+1} Q_{u,r}^{n+1} \\ -Q_{d,r}^{n+1} & -\alpha_3 w_u^{n+1} Q_{d,r}^{n+1} & \alpha_0 + \alpha_3 w_u^{n+1} Q_{u,r}^{n+1} \end{bmatrix} \tag{31}$$

where $\left|\mathbf{M}_r^{n+1}\right| = \alpha_0 + \alpha_3(w_u^{n+1} Q_{u,r}^{n+1} + w_d^{n+1} Q_{d,r}^{n+1})$ and

$$Q_{\nu,r}^{n+1} = \sum_{l=1}^{L_\nu} \theta_{\nu l} \Psi_{\nu l}(n) \exp\left\{-\frac{(V_{L,r}^{n+1} - c_{\nu l}^0)^2}{2\beta_\nu^2}\right\}\left(\frac{V_{L,r}^{n+1} - c_{\nu l}^0}{\beta_\nu^2}\right), \quad \nu = u, l. \tag{32}$$

We remark that (29), due to the adopted RBF model representation, represents a very smooth multivariate function. Therefore, very few iterations are required for reaching stringent accuracies. This will be demonstrated in the numerical examples of Section VI.

VI. Numerical Results

This section presents a set of numerical examples showing the high accuracy of the proposed modeling strategy for full-wave analysis of interconnected digital I/O ports. The examples to be discussed are intended to provide separate validations for all the modeling steps as well as to illustrate the feasibility of the proposed technique for realistic applications.

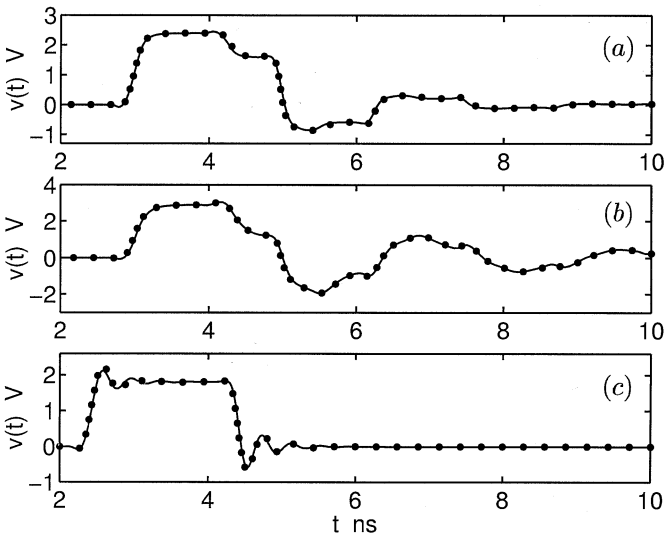

Fig. 2. Far-end voltage waveform $v(t)$ on three ideal transmission lines driven by a commercial digital driver. Solid lines: reference; dotted lines: macromodel. Panel (*a*) refers to a line with $Z_c = 50\,\Omega$, $T_d = 0.6$ ns; (*b*) $Z_c = 100\,\Omega$, $T_d = 0.6$ ns; (*c*) $Z_c = 100\,\Omega$, $T_d = 40$ ps.

A. RBF Macromodeling

The first numerical test provides an example of RBF macromodeling for the the characterization of the output port of a commercial device, namely a high-speed CMOS driver (power supply: $V_{ss} = 0$ V, $V_{dd} = 1.8$ V) used in IBM mainframe products. The macromodel is derived from the transistor-level model of the driver by applying the procedure discussed in [18]. The RBF macromodel (17) turns out to have a dynamic order $r = 2$ with submodels i_u^m and i_d^m requiring a number of 12 and 10 basis functions, respectively. The sampling time used in the identification process is $T_s = 10$ ps.

In order to assess the accuracy and efficiency of the estimated macromodel, we used SPICE as the simulation engine and implemented the estimated macromodel as a SPICE subcircuit. The circuit interpretation and the SPICE implementation of (17) is out of the scope of this paper and can be found in [18]. As a validation test, Fig. 2 compares the responses of the driver when it applies a 4-ns pulse (bit pattern "010") to three ideal transmission lines, with different characteristic impedance and time delay values, terminated by a 1-pF capacitor. The accuracy of the macromodel in reproducing the reference behavior of the actual device for generic dynamic loads can be clearly appreciated. We remark that transient simulation of the the estimated macromodel results more than 20 times faster than for the original transistor-level model.

$$\begin{cases} \alpha_0 V_L^{n+1} - \alpha_1 V_L^n + \alpha_2 \left[\hat{z} \cdot \nabla \times \mathbf{H}\right]_{ijk}^{n+1/2} \\ \qquad -\alpha_3 \left(w_u^{n+1} I_u^{n+1} + w_d^{n+1} I_d^{n+1}\right) - \alpha_3 \left(w_u^n I_u^n + w_d^n I_d^n\right) &= 0 \\ I_u^{n+1} - \sum_{l=1}^{L_u} \theta_{ul} \Psi_{ul}(n) \exp\left\{-\frac{(V_L^{n+1} - c_{ul}^0)^2}{2\beta_u^2}\right\} &= 0 \\ I_d^{n+1} - \sum_{l=1}^{L_d} \theta_{dl} \Psi_{dl}(n) \exp\left\{-\frac{(V_L^{n+1} - c_{dl}^0)^2}{2\beta_d^2}\right\} &= 0 \end{cases} \tag{29}$$

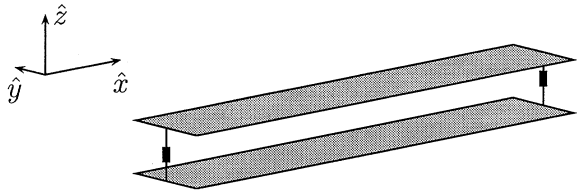

Fig. 3. Transmission-line structure used for validation. The sketch is not to scale (see text for dimensions). The lumped terminations are indicated as thick lines.

The input port of this device can also be used as a receiver, and a RBF macromodel can be correspondingly derived. Therefore, we will extensively use this device in the numerical examples to be presented next. For brevity, we omit the validation curves for such receiver model. Such curves, together with additional details on the derivation, may be found in [18].

B. RBF-FDTD Validation

The present example is intended to validate the various steps required by the mixed RBF-FDTD modeling procedure. These steps are

1) derivation of the discrete-time macromodel from the specific device under consideration;
2) model resampling for time step matching;
3) FDTD implementation.

The structure that we chose for validation is a simple transmission line depicted in Fig. 3. The computational domain is $180 \times 24 \times 23$ cells, with mesh size $\Delta x = \Delta y = \Delta z = 0.723$ mm, and is terminated by absorbing boundary conditions. The strips are implemented as zero-thickness conductors and are four cells wide and 160 cells long. The separation between the two strips is three cells. The effective characteristic impedance of the resulting transmission line is $Z_c \sim 131\ \Omega$, while the line delay is $T_D \sim 0.4$ ns. The line is terminated at the near end by the lumped RBF macromodel for the driver detailed in Section VI-A. The driver forces a bit pattern "010" at its output port, with a bit time of 2 ns. The far end termination is varied in order to illustrate load insensitivity of the proposed modeling strategy.

We consider first the case of a linear capacitive far end termination made of a shunt connection of a 1-pF capacitor and a 500-Ω resistor. The simulation results are depicted in Fig. 4, where four different curves are plotted for near-end and far-end voltage. The first curve is the result of a SPICE simulation using the transistor-level model of the driver. This can be regarded as the reference curve. The second curve is obtained always with SPICE but using the RBF model of the driver. This can be regarded as a validation for step 1 above. The third curve is the result of a FDTD simulation of the [one-dimensional (1-D)] telegraphers equations using the RBF model. The implementation of the model as a lumped termination of the 1-D FDTD mesh is a standard procedure and is not further commented here. The reader is referred to [11] for a detailed discussion. This curve is intended to validate the FDTD implementation, the resampling strategy, and the iterative nonlinear solver without the influence of spurious numerical dispersion occurring in 3-D FDTD. Finally, the fourth curve shows the result of the full-wave simulation. The latter was performed with the maximum allowed time

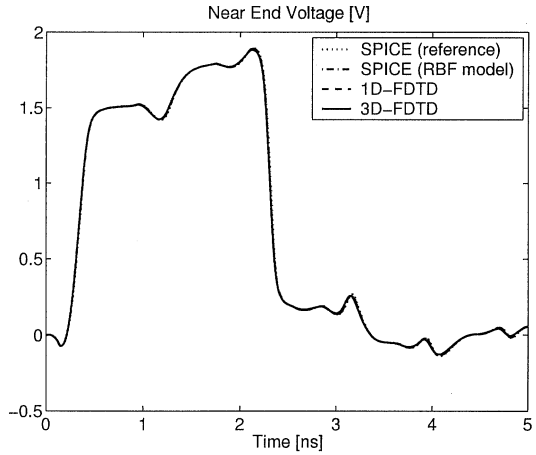

(a)

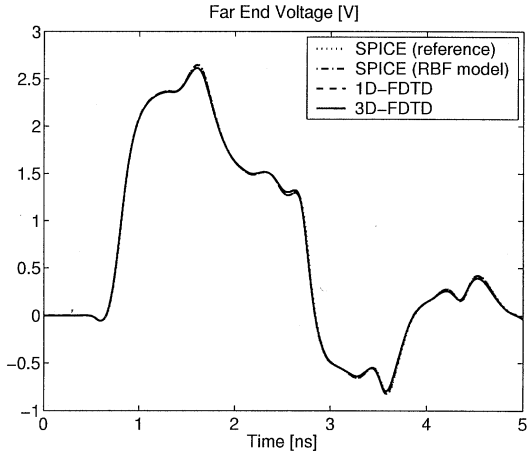

(b)

Fig. 4. Termination voltages with switching driver at near end and capacitive load at far end. See text for additional details.

step $\Delta t \sim 1.39$ ps. Since the sampling time used for identification of the RBF model was $T_s = 10$ ps, the resulting resampling factor is $\tau = 0.139$. As expected, the four curves are almost undistinguishable. Only the 3-D FDTD result has a marginal deviation from the other curves due to numerical dispersion. We remark that the number of Newton-Raphson iterations required to solve the RBF model (29) never exceeded a maximum number of three, whereas the accuracy threshold was set to the very stringent value of 10^{-9}. Note that the FDTD (linear) computations were performed in single-precision arithmetic, while double-precision was used for the nonlinear RBF computations.

The second example considers a fully dynamic/nonlinear termination at the far end, namely the RBF model of the receiver discussed in Section VI-A. Fig. 5 shows near and far end voltages, reporting only the response computed by SPICE using the RBF model and the result of full-wave FDTD simulation. Again, the two curves are almost undistinguishable apart from minimal dispersion effects.

The final validation example illustrates the capability of modeling the effects of an impinging wave. The structure is identical to the above, with the switching driver at the near end and the linear capacitive load at the far end. In addition, a plane wave with Gaussian waveform is incident broadside on the structure,

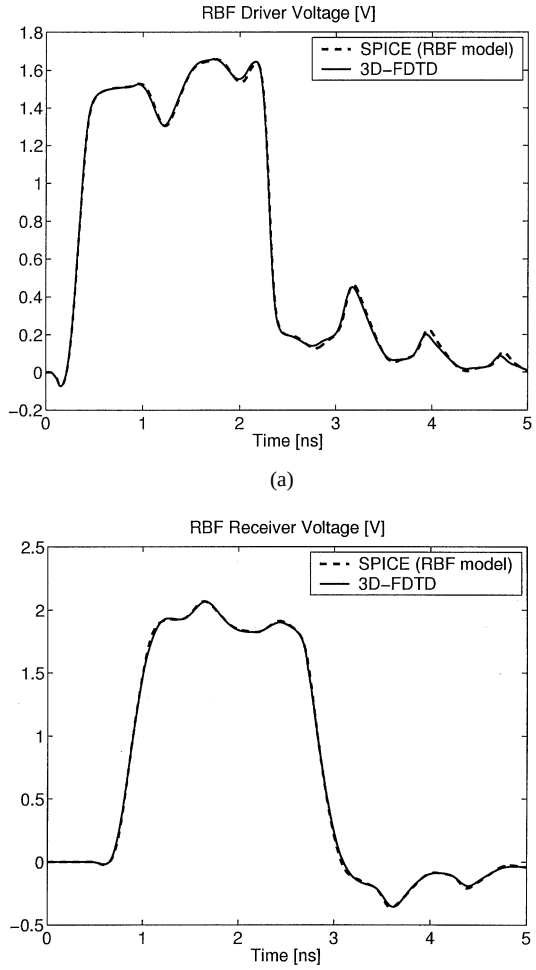

Fig. 5. Termination voltages with switching driver at near end and receiver at far end.

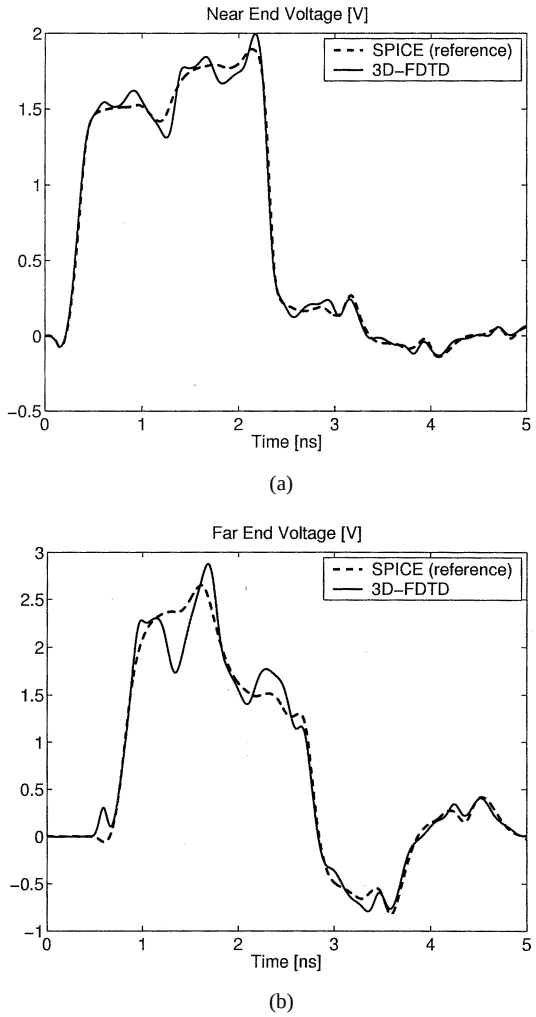

Fig. 6. Termination voltages with switching driver at near end, capacitive load at far end, and incident field. Reference solution is computed without incident field contribution.

i.e., from a direction $\{\theta = 90°, \varphi = 90°\}$ with θ-polarized electric field in standard spherical coordinates. The amplitude of the Gaussian is 500 V/m, and the width is 0.35 ns. Fig. 6 reports the results, showing the unperturbed driver voltage waveforms (using SPICE with transistor-level model) and the field-perturbed waveforms obtained by FDTD.

C. EMI on a Loaded PCB Structure

We turn now to a more realistic application. The 5×5-cm PCB structure depicted in Fig. 7 is considered. This configuration is similar to the one analyzed in [3]. Three 400 μm-wide coupled strips run parallel to each other on the top (along x coordinate, length 4 cm) and bottom (along y coordinate, length 4 cm) of the PCB signal layer. Three vias connect the orthogonal sections of the strips. Top and bottom glue layers cover the signal layer, and the entire PCB is metallized on both sides. The relative permettivity for all layers is $\varepsilon_r = 4.3$, with a single layer height of 400 μm. The innermost strip is driven by the RBF macromodel of the driver on one end and is terminated on the other end by the RBF macromodel of the receiver. All the other terminations consist of 50-Ω resistors. The driver forces a "010" bit sequence at its output port. In addition, an external

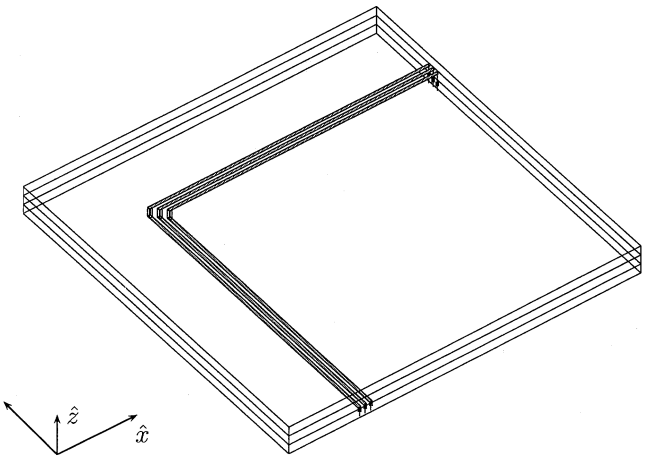

Fig. 7. PCB structure for illustration of incident field coupling. The picture is not to scale (see text for board dimensions).

wave pulse impinges on the structure from a direction $\{\theta = 90°, \varphi = 180°\}$ with a θ polarized electric field in standard spherical coordinates. The amplitude of the pulse is 2 kV/m, with a bandwidth of 9.2 GHz. Fig. 8 shows the termination voltages and

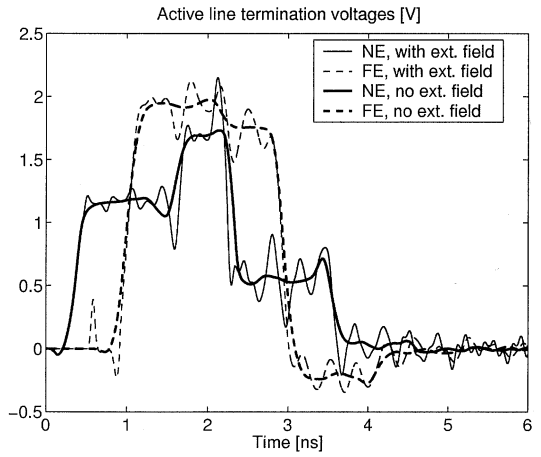

(a)

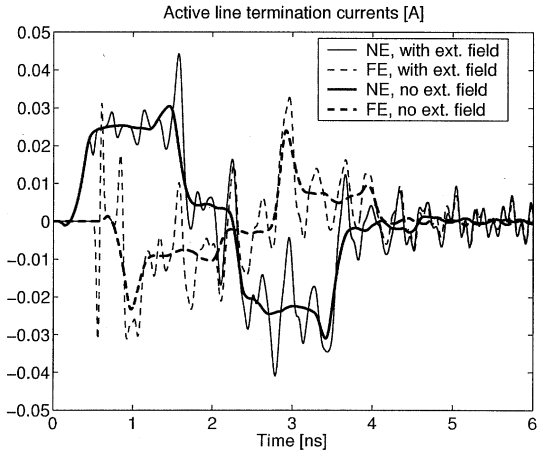

(b)

Fig. 8. Termination voltages and currents for the PCB structure of Fig. 7 with and without incident field contribution (NE, near end; FE, far end).

currents for the driven line with and without incident field. This example illustrates that the proposed modeling strategy can be employed for the complex task of predicting incident-field coupling effects on interconnected networks loaded by real-world components.

VII. Conclusion

A systematic procedure for the full-wave modeling of interconnected digital I/O ports has been presented. The proposed modeling strategy is based on the implementation of nonlinear dynamic macromodels of digital ports as lumped elements into a full-wave FDTD solver. The port macromodels that have been considered are discrete-time behavioral models based on RBF expansions. Such models have a solid theoretical foundation and are shown to provide efficient and extremely accurate representations of the port behavior for digital drivers and receivers. A rigorous stability analysis has been performed, showing that time-step matching between port macromodel and FDTD sampling times can be achieved through a simple resampling strategy. This procedure does not spoil the accuracy of the entire modeling task. A set of numerical examples has demonstrated the feasibility of the proposed approach.

Appendix
Stability

Stability is a fundamental feature since it allows to damp the unavoidable numerical errors occurring at each time iteration. We split the stability analysis in two parts. First, the intrinsic stability of the RBF macromodels before resampling is addressed in Section A. Second, the effects of resampling are investigated in Section B. Since the initial RBF macromodels are stable and since this stability is preserved by the resampling procedure, we conclude that the proposed hybridization of discrete-time models for digital I/O ports and FDTD results stable.

A. Stability of RBF Macromodels

This section discusses the intrinsic stability of the discrete-time macromodels for digital drivers and receivers before applying the resampling procedure. The general functional form of such models is detailed in (12), with the internal discrete-time states defined by (13). It should be noted that RBF macromodels are constructed so that their transient response is the same as for the actual device. Therefore, the stability of a discrete-time macromodel is determined by the behavior of the detailed transistor-level model for the device under consideration. This model must always be stable by definition, being the starting point of all subsequent approximation steps.

The stability of some macromodel can only be assessed under given loading conditions. Therefore, we will consider a resistive load having fixed conductance G_L. The discrete-time system under consideration becomes

$$\begin{cases} i^m = & F(\boldsymbol{\Theta}; \mathbf{x}_i^{m-1}, v^m, \mathbf{x}_v^{m-1}; m) \\ i^m = & G_L v^m \,. \end{cases} \tag{33}$$

This is an implicit discrete-time dynamical system that can be solved for port voltage and current at each time iteration, e.g., by Newton–Raphson algorithm. The stability analysis can be conveniently carried out if we are able to restate this system in explicit form, i.e.

$$\mathbf{x}^m = \mathbf{G}(\mathbf{x}^{m-1}; m) \tag{34}$$

where the global state vector collects the current and voltage states

$$\mathbf{x}^m = \begin{bmatrix} \mathbf{x}_i^m \\ \mathbf{x}_v^m \end{bmatrix} . \tag{35}$$

The parameters set $\boldsymbol{\Theta}$ is omitted for the sake of clarity. Note that the nonlinear multivariate function $\mathbf{G}$ depends also on the time iteration m in order to account for the time-varying nature of digital drivers. Also, since F is assumed in this paper to be an RBF expansion using exponentials as elementary blocks, F is continuously differentiable an arbitrary number of times. Consequently, $\mathbf{G}$ is continuously differentiable provided that system (33) has a unique solution. This result is important for the forthcoming discussion.

Stability guarantees that the unavoidable numerical errors occurring at each time iteration are not amplified by the dy-

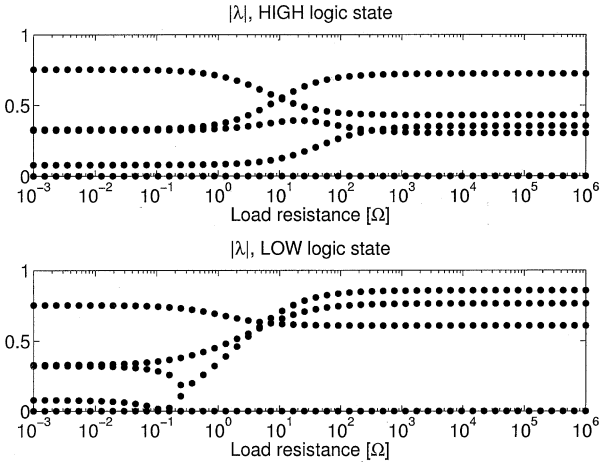

Fig. 9. Eigenspectrum (magnitude) of linearized system around the equilibirum point at HIGH (top panel) and LOW (bottom panel) logic states, for various load conditions.

namics of the model. We consider then, the following perturbed problem:

$$\begin{cases} \mathbf{z}^m = & \mathbf{G}(\mathbf{z}^{m-1}; m) \\ \mathbf{z}^{m-1} = & \mathbf{x}^{m-1} + \delta\mathbf{x}^{m-1} \end{cases} \tag{36}$$

where the term $\delta\mathbf{x}^{m-1}$ denotes the numerical approximation error at iteration $m-1$. Assuming that the perturbed system above is solved exactly at iteration m, we can define the evolution of the approximation error as

$$\delta\mathbf{x}^m = \mathbf{z}^m - \mathbf{x}^m = \mathbf{G}(\mathbf{x}^{m-1} + \delta\mathbf{x}^{m-1}; m) - \mathbf{G}(\mathbf{x}^{m-1}; m)\,. \tag{37}$$

Due to the differentiability of $\mathbf{G}$ we can expand to first order this expression

$$\delta\mathbf{x}^m = \mathbf{M}(\mathbf{x}^{m-1}; m)\,\delta\mathbf{x}^{m-1} + \mathcal{O}(||\delta\mathbf{x}^{m-1}||^2) \tag{38}$$

where $\mathbf{M}$ is the Jacobian matrix of $\mathbf{G}$. Stability is guaranteed when all the eigenvalues of $\mathbf{M}$ satisfy

$$|\lambda_k| < 1 \qquad \forall k\,. \tag{39}$$

We use this criterion to test for stability the RBF macromodels used in this paper.

The first test shows that the nonswitching driver fixed either in the HIGH or LOW logic state is always stable regardless of the load conditions. If the driver is in a fixed state the connection with a resistive load leads to a single equilibrium (steady-state) point depending on the load

$$\mathbf{x}^m = \mathbf{x}^{m-1} = \mathbf{x}_Q(G_L) \tag{40}$$

since both F and $\mathbf{G}$ do not depend on the time iteration m. The Jacobian matrix and its eigenspectrum can then be computed at this steady-state point in order to characterize its stability. Fig. 9 reports the magnitude of all eigenvalues for the driver under consideration in both logic states, plotted as functions of the load resistance. Steady states are stable since all eigenvalues satisfy criterion (39).

The next test illustrates the time-dependent eigenspectrum for the switching driver. A bit pattern "010" is forced at the output

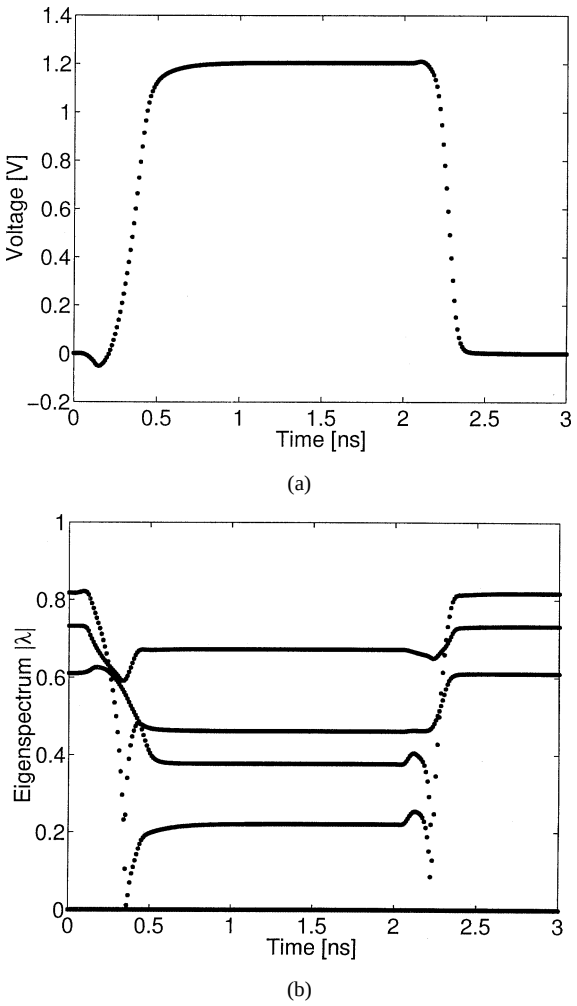

Fig. 10. Switching voltage waveform (50-Ω load resistance) for "010" bit pattern (left panel) and corresponding eigenspectrum (magnitude) of linearized system.

of the driver through appropriate time-dependent weight functions. A 50-Ω resistive load is connected to the driver and a discrete-time simulation is run. At each time iteration the Jacobian matrix $\mathbf{M}$ and its eigenvalues are computed. The result is shown in Fig. 10. The left panel reports the discrete-time voltage waveform at the driver output. The right panel depicts the magnitude of all eigenvalues at each time iteration. Also, in the dynamic case, we see that no eigenvalue exceeds one, therefore all numerical errors get damped as the simulation proceeds. We remark that the same qualitative results are obtained with any load resistance connected to the driver.

B. Resampling and Stability

This section investigates the time stability of the resampled macromodels derived in Section IV. We show in the following that the time conversion steps leading to the resampled model preserve stability. Therefore, if the original macromodel is stable, the resampled one will also be stable.

Stability of resampling is best illustrated by the behavior of a standard test problem, namely

$$\hat{\zeta}^{m+1} = \lambda\,\hat{\zeta}^m, \qquad |\lambda| < 1\,. \tag{41}$$

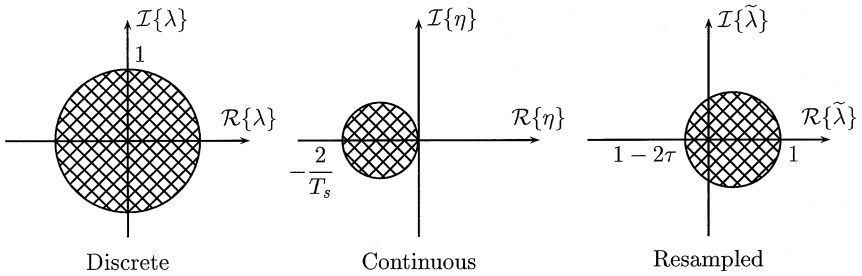

Fig. 11. Stability of the time conversion applied to the linear test problem. The three panels show the eigenvalues of the discrete, continuous, and resampled test problem.

The results presented in Appendix A show that the above test problem is appropriate since all the eigenvalues associated to the original RBF model before resampling have magnitude less than one, i.e., the criterion in (39) is unconditionally satisfied. If we now apply the proposed discrete-to-continuous time conversion procedure we get

$$\frac{d}{dt}\zeta(t) = \eta\,\zeta(t)\,, \qquad \eta = \frac{\lambda - 1}{T_s} \tag{42}$$

where a first-order forward approximation of the time derivative has been used. The relationship between discrete and continuous state variables is $\zeta(mT_s) \simeq \widehat{\zeta}^m$ with first-order accuracy. Due to the stability constraint on the original system (41) we conclude that the eigenvalue η of the continuous system has negative real part, allowing us to prove stability. Applying now the continuous-to-discrete time approximation with samplimg time Δt, and using again a first-order forward difference approximation, we get the resampled system

$$\widetilde{\zeta}^{n+1} = \widetilde{\lambda}\,\widetilde{\zeta}^n\,, \qquad \widetilde{\lambda} = 1 + \tau(\lambda - 1)\,. \tag{43}$$

Fig. 11 depicts the region of the complex plane with possible values of $\widetilde{\lambda}$, i.e., a circle centered at $(1-\tau)$ with radius τ. Stability is guaranteed when $|\widetilde{\lambda}| < 1$, i.e., when the resampling factor satisfies

$$\tau \leq 1\,. \tag{44}$$

This is quite natural since the overall resampling process can be interpreted as the application of a linear interpolation scheme. If the resampling factor becomes larger than one this scheme becomes an extrapolation, which is always to be avoided. Also, due to the usual size of the interconnect structures where the devices under investigation can be found, the required cell size for FDTD must be very small in order to describe the geometry with sufficient accuracy. Therefore, the resulting time step Δt is generally much smaller than the time scale of typical driver/receiver responses. We conclude that the requirement of (44) is not restrictive in any case of practical interest.

ACKNOWLEDGMENT

The authors are grateful to G. Katopis, D. Becker, and Z. Chen (IBM Enterprise System Group, Poughkeepsie, NY) for providing the drivers and receivers data that we employed for the generation of RBF macromodels, and for validations.

REFERENCES

[1] S. Chen, C. F. N. Cowan, and P. M. Grant, "Ortogonal least squares learning algorithm for radial basis function network," *IEEE Trans. Neural Networks*, vol. 2, pp. 302–309, Mar. 1991.

[2] A. Dounavis, E. Gad, R. Achar, and M. Nakhla, "Passive model reduction of multiport distributed interconnects," *IEEE Trans. Microwave Theory Tech.*, vol. 48, pp. 2325–2334, Dec. 2000.

[3] I. Erdin, M. Nakhla, and R. Achar, "Circuit analysis of electromagnetic radiation and field coupling effects for networks with embedded full-wave modules," *IEEE Trans. Electromagn. Compat.*, vol. 42, pp. 449–460, Nov. 2000.

[4] (1999) I/O Buffer Information Specification (IBIS) Ver. 3.2. [Online]. Available: http://www.eigroup.org/ibis/ibis.htm

[5] K. Judd and A. Mees, "On selecting models for nonlinear time series," *Physics D*, vol. 82, pp. 426–444, 1995.

[6] M. Li, X. Luo, and J. L. Drewniak, "FDTD modeling of lumped ferrites," *IEEE Trans. Electromagn. Compat.*, vol. 42, pp. 152–151, May 2000.

[7] L. Ljung, *System Identification: Theory for the User*. Englewood Cliffs, NJ: Prentice-Hall, 1987.

[8] K. S. Kunz and R. J. Luebbers, *The Finite-Difference Time-Domain Method for Electromagnetics*. Boca Raton, FL: CRC, 1994.

[9] C. Kuo, B. Houshmand, and T. Itoh, "Full-wave analysis of packaged microwave circuits with active and nonlinear devices: An FDTD approach," *IEEE Trans. Microwave Theory Tech.*, vol. 45, pp. 819–826, May 1997.

[10] A. Odabasioglu, M. Celik, and L. T. Pileggi, "PRIMA: Passive reduced-order interconnect macromodeling algorithm," *IEEE Trans. Computer-Aided Des.*, vol. 17, pp. 645–654, Aug. 1998.

[11] C. R. Paul, "Incorporation of terminal constraints in the FDTD analysis of transmission lines," *IEEE Trans. Electromagn. Compat.*, vol. 36, pp. 85–91, May 1994.

[12] J. A. Pereda, F. Alimenti, P. Mezzanotte, L. Roselli, and R. Sorrentino, "A new algorithm for the incorporation of arbitrary linear lumped networks into FDTD simulations," *IEEE Trans. Microwave Theory Tech.*, vol. 47, pp. 943–949, June 1999.

[13] M. Piket-May, A. Taflove, and J. Baron, "FD-TD modeling of digital signal propagation in 3-D circuits with passive and active loads," *IEEE Trans. Microwave Theory Tech.*, vol. 42, pp. 1514–1523, Aug. 1994.

[14] I. W. Sandberg, "Approximations for nonlinear functionals," *IEEE Trans. Circuits Syst. I*, vol. 39, pp. 65–67, Jan. 1992.

[15] ——, "Approximation theorems for discrete-time systems," *IEEE Trans. Circuits Syst.*, vol. 38, pp. 564–566, May 1991.

[16] C. Schuster and W. Fichtner, "Parasitic modes on printed circuit boards and their effects on EMC and signal integrity," *IEEE Trans. Electromagn. Compat.*, vol. 43, pp. 416–425, Nov. 2001.

[17] J. Sjöberg *et al.*, "Nonlinear black-box modeling in system identification: A unified overview," *Automatica*, vol. 31, no. 12, pp. 1691–1724, 1995.

[18] I. S. Stievano, F. G. Canavero, and I. A. Maio, "Parametric macromodels of digital I/O ports," *IEEE Trans. Adv. Packag.*, pp. 255–264, May 2002.

[19] I. S. Stievano, Z. Chen, D. Becker, F. G. Canavero, G. Katopis, and I. A. Maio, "Macromodeling of digital I/O ports for system EMC assessment," in *Proc. Design, Automation, Test Eur. Conf.*, Paris, France, Mar. 4–8, 2002.

[20] I. S. Stievano and I. A. Maio, "Behavioral models of digital IC ports from measured transient waveforms," in *Proc. 9th IEEE Topical Meeting on Electrical Performance of Electronic Packaging*, Oct. 2000, pp. 211–214.

[21] W. Sui, D. A. Christensen, and C. H. Durney, "Extending the two-dimensional FDTD method to hybrid electromagnetic systems with active and passive lumped elements," *IEEE Trans. Microwave Theory Tech.*, vol. 40, pp. 724–730, Apr. 1992.

[22] A. Taflove, *Computational Electrodynamics: The Finite-Difference Time-Domain Method*. Norwood, MA: Artech House, 1995.
[23] B. Houshmand, T. Itoh, and M. Piket-May, "High-speed electronic circuits with active and nonlinear components," in *Advances in Computational Electrodynamics: The Finite-Difference Time-Domain Method*, A. Taflove, Ed. Norwood, MA: Artech House, 1998, ch. 8.
[24] Y.-S. Tsuei, A. C. Cangellaris, and J. Prince, "Rigorous electromagnetic modeling of chip-to-package (first-level) interconnections," *IEEE Trans. Comp., Packag., Manufact. Technol.*, vol. 16, pp. 876–883, Dec. 1993.
[25] J. Vlach and K. Singhal, *Computer Methods for Circuit Analysis and Design*. New York: Van Nostrand, 1983.
[26] X. Ye and J. L. Drewniak, "Incorporating two-port networks with S-parameters into FDTD," *IEEE Microwave Wireless Comp. Lett.*, vol. 11, no. 2, pp. 77–79, 2001.
[27] K. S. Yee, "Numerical solution of initial boundary value probems involving Maxwell's equations in isotropic media," *IEEE Trans. Antennas Propagat.*, vol. AP-14, pp. 302–307, 1966.

Stefano Grivet-Talocia received the Laurea and Ph.D. degrees in electronic engineering from the Polytechnic University of Turin, Turin, Italy, in 1994 and 1998, respectively.

From 1994 to 1996, he was at NASA/Goddard Space Flight Center, Greenbelt, MD, where he worked on applications of fractal geometry and wavelet transform to the analysis and processing of geophysical time series. Currently, he is an Associate Professor of Circuit Theory with the Department of Electronics, Polytechnic University of Turin. His current research interests are in numerical modeling of interconnects, applications of wavelets to computational electromagnetics, and macromodeling of lumped and distributed structures.

From 1999 to 2001, he served as Associate Editor for the IEEE TRANSACTIONS ON ELECTROMAGNETIC COMPATIBILITY.

Igor S. Stievano received the Laurea and Ph.D. degrees in electronic engineering from the Polytechnic University of Turin, Turin, Italy, in 1996 and in 2001, respectively.

Currently he is an Assistant Researcher with the Department of Electronics, Polytechnic University of Turin. His research activity is on the modeling of nonlinear circuit elements with specific application to the behavioral characterization of digital integrated circuits for the assesment of signal integrity and electromagnetic compatibility effects.

Flavio G. Canavero (M'90–SM'99) received the Laurea degree in electronic engineering from the Polytechnic University of Turin, Turin, Italy, in 1977, and the Ph.D. degree from the Georgia Institute of Technology, Atlanta, in 1986.

Currently, he is a Professor of Circuit Theory and Electromagnetic Compatibility with the Department of Electronics, Polytechnic University of Turin, Turin, Italy. His research interests are in the field of electromagnetic compatibility, where he works on line modeling and digital integrated circuits characterization for signal integrity, field coupling to multiwire lines, and statistical methods in EMC.

He is the VP for Organization of his University, and the Managing Editor for the IEEE TRANSACTIONS ON ELECTROMAGNETIC COMPATIBILITY and the Chair of the Workshop on signal propagation on interconnects (SPI).